Full length article

Strain gradient plasticity-based modeling of hydrogen environment assisted cracking

Emilio Martínez-Pañeda [a], [*], Christian F. Niordson [b], Richard P. Gangloff [c]

[a] Department of Construction and Manufacturing Engineering, University of Oviedo, Gijón 33203, Spain
[b] Department of Mechanical Engineering, Solid Mechanics, Technical University of Denmark, Kgs. Lyngby DK-2800, Denmark
[c] Department of Materials Science and Engineering, University of Virginia, Charlottesville, VA 22904, USA

A B S T R A C T

Finite element analysis of stress about a blunt crack tip, emphasizing finite strain and phenomenological and mechanism-based strain gradient plasticity (SGP) formulations, is integrated with electrochemical assessment of occluded-crack tip hydrogen (H) solubility and two H-decohesion models to predict hydrogen environment assisted crack growth properties. SGP elevates crack tip geometrically necessary dislocation density and flow stress, with enhancement declining with increasing alloy strength. Elevated hydrostatic stress promotes high-trapped H concentration for crack tip damage; it is imperative to account for SGP in H cracking models. Predictions of the threshold stress intensity factor and H-diffusion limited Stage II crack growth rate agree with experimental data for a high strength austenitic Ni-Cu superalloy (Monel®K-500) and two modern ultra-high strength martensitic steels (AerMet™100 and Ferrium™M54) stressed in 0.6 M NaCl solution over a range of applied potential. For Monel®K-500, K_{TH} is accurately predicted versus cathodic potential using either classical or gradient-modified formulations; however, Stage II growth rate is best predicted by a SGP description of crack tip stress that justifies a critical distance of 1 μm. For steel, threshold and growth rate are best predicted using high-hydrostatic stress that exceeds 6 to 8 times alloy yield strength and extends 1 μm ahead of the crack tip. This stress is nearly achieved with a three-length phenomenological SGP formulation, but additional stress enhancement is needed, perhaps due to tip geometry or slip-microstructure.

© 2016 Acta Materialia Inc. Published by Elsevier Ltd. All rights reserved.

1. Introduction

Multi-scale model predictions of material properties are important for alloy and process development, material life-cycle optimization, and component performance prognosis [1]. Interdisciplinary advances in deformation processing [2], fatigue [3], stress corrosion cracking (SCC) [4], and hydrogen embrittlement [5] illustrate this cutting-edge approach. Internal hydrogen and hydrogen environment assisted cracking (IHAC and HEAC, respectively) degrade high toughness alloys in fracture-critical aerospace, ship, energy, and ground transportation structures [6]. Moreover, hydrogen-stimulated damage is a primary mechanism for SCC of titanium, iron, nickel and aluminum-based alloys [7]. Models based on hydrogen-enhanced decohesion (HEDE) [8], interacting with hydrogen-enhanced localized

plasticity (HELP) [9], predict trends in the subcritical crack growth rate properties of alloys stressed in environments that produce atomic hydrogen (H) via chemical and electrochemical reactions on crack tip surfaces [7,10]. However, improvements are required; local crack tip stress and dislocation configuration, as well as crack opening profile, are particularly important [11,12].

Building on elastic stress intensity factor (K) similitude for subcritical crack propagation [10], a diversity of IHAC and HEAC models [13–21] employ a crack tip stress field from classical continuum fracture mechanics [10,22], including finite-strain blunting [23], to predict growth threshold (K_{TH}) and rate (da/dt) properties. Alternative modeling is based on dislocation shielding of elastic crack tip stresses [24–27]. The difference between these two approaches centers on the magnitude and distribution of crack tip stresses, which define the location and severity of crack tip H-damage in the fracture process zone (FPZ). Continuum plasticity modeling shows that the maximum opening-direction tensile stress is 3–5 times alloy yield strength and located at 1–2 blunted

crack tip opening displacements (of order 2–20 μm) ahead of the crack tip surface [23]. Dislocation-based models predict crack opening-direction stresses of 12–25 times yield strength and located much closer to the crack tip [24,25]. This difference is important because HEDE defines cracking as the balance between local tensile stress and H-concentration-reduced interface strength [8] (or reduced-total work of fracture [14,15]). Crack tip H concentration increases exponentially with rising hydrostatic stress [28,29], the crack tip stress gradient affects H diffusion [20,21], and dislocation density impacts the H flux via reversible-H trapping [21]. Next generation H-cracking models require an improved-quantitative description of the crack tip stress field between the extremes represented by classical continuum plasticity and dislocation shielding.

Extensive research has focused on the *smaller is harder* behavior of metals [30–35]. This size effect is attributed to geometrically necessary dislocations (GNDs), which accommodate lattice curvature due to non-uniform plastic deformation. Since classical plasticity lacks a material length, strain gradient plasticity (SGP) theories have been proposed to capture size effects. Isotropic SGP formulations are phenomenological (PSGP) [31] or mechanism-based (MSGP) [33,34]. These theories bridge the gap between length-independent continuum plasticity and discrete dislocation modeling by linking statistically stored and geometrically necessary dislocation densities to the mesoscale plastic strain/strain gradient and strain hardening. Since the plastic zone is small, with a large spatial gradient of high-strain deformation [23], it is imperative to account for GNDs in modeling crack tip stress and strain. Critically important for IHAC and HEAC, SGP modeling has consistently shown that increased GND density at the crack tip leads to: (a) higher local stresses, (b) a contraction in the breadth of the crack tip stress distribution, and (c) reduced blunting; each compared to classical plasticity [36–38]. SGP must be quantitatively implemented in material-damage models [39], as recognized for cleavage [40], interface fracture [41], layered-structure damage [42], ductile-microvoid fracture [43], fatigue [44], and H-enhanced cracking [7,45].

Recent SGP advances are relevant to finite element analysis (FEA) of crack tip stress and strain. PSGP theory with the full complement of three-gradient terms predicts high stresses that persist to a 10-fold larger distance ahead of the sharp crack tip compared to predictions from a single-length formulation [36]. However, this FEA was based on infinitesimal strain [31,36]. A large-strain FEA analysis of a blunting crack tip demonstrated that PSGP and MSGP formulations each predict elevated crack tip tensile stress and reduced crack tip opening compared to classical plasticity [37,38]. The distance over which this stress elevation persists is up to tens of micro-meters, sufficient to engulf the FPZ for HEAC [7], before merging with classical predictions at larger distances within the plastic zone. While classical plasticity predicts a stress maximum located at 1–2 blunted openings in front of the crack tip [22,23], large-strain SGP-enhanced stresses are highest at the smallest-FEA-modeled distance (100 nm) ahead of the tip, with no evidence of a stress maximum. Finally, SGP promotes stress elevation that depends on applied load, in sharp contrast to the K_I independence of maximum stress predicted by classical plasticity [23]. The crack tip stress distribution is affected by both the SGP model used and value(s) of the material length(s). Uncertainties remain regarding: (a) the constitutive prescription that best captures increased GND density associated with a plastic strain gradient [32], and (b) the absolute values of material-dependent length(s) dependent on test method (e.g., nano-indentation) and SGP-model analysis of such measurements [36,38].

2. Objective

The objective of this research is to implement and validate the coupling of a large-strain FEA-SGP analysis of crack tip stress with HEDE-mechanism-based models that predict HEAC propagation threshold and kinetics properties. Specific aims are to: (1) improve the basis for HEAC models using SGP inputs and insights, (2) predict H-cracking properties with fewer model parameters, (3) contribute insight into the role of GNDs ahead of a crack tip, and (4) experimentally assess the proper continuum-SGP formulation of crack tip stresses.

Model assessment is based on measurements of da/dt versus K_I for HEAC in a Ni-Cu superalloy [46,47] and two ultra-high strength martensitic steels [48,49], each stressed in a chloride solution. Electrochemistry measurements and modeling yielded diffusible crack tip H concentration versus bold-surface applied potential (E_{APP}) [46,50], as well as trap-affected effective H diffusivity (D_{H-EFF}) for each alloy [51–53]. The E_{APP} dependencies of K_{TH} and the H-diffusion limited Stage II crack growth rate (da/dt$_{II}$) were originally modeled [46–49] using crack tip stress expected from blunt-crack [23] and dislocation shielding [24] analyses. This database and the HEDE-modeling approach are reanalyzed using crack tip stress distributions from new FEA that incorporates: (a) the finite strain framework for both PSGP and MSGP [38], and (b) specific alloy-dependent properties and load levels that create H cracking.

3. Experimental procedure

Three high strength alloys were modeled: (a) an austenitic Ni-Cu superalloy hardened by spherical γ′ precipitates (Ni₃(Al,Ti); 5 nm radius, 0.08–0.1 vol fraction, and 150000 to 190000 precipitates/μm³ [54]), and (b) two martensitic ultra-high strength steels strengthened by needle-shaped carbide precipitates ((Cr,Mo)₂C; 1 nm radius, 5–8 nm length, volume fraction of order 0.03, and about 150000 precipitates/μm³ [52,55,56]). The heat treatment and microstructure of the superalloy, Monel®K-500 (Ni-28.6Cu-2.89Al-0.45Ti-0.166C by wt pct), are described elsewhere [46,51,54]: 0.2% offset yield strength (σ_{YS}) is 773 MPa, elastic modulus (E) is 183.9 GPa, and ultimate tensile strength (σ_{UTS}) is 1169 MPa from tensile testing; Ramberg-Osgood flow constants [57] from compression testing are n = 20, α = 0.39, E = 185.7 GPa and $\sigma_o = \sigma_{YSc}$ = 786 MPa; and plane strain fracture toughness (K_{IC}) is 200–340 MPa√m. The two similar quenched and aged block-martensitic alloy steels, AerMet™100 (Fe-13.4Co-11.1Ni-3.0Cr-1.2-Mo-0.23C by wt pct) and Ferrium™M54 (Fe-7.0Co-10.1Ni-1.0Cr-2.1Mo-1.3-W-0.1V-0.30C by wt pct), are described elsewhere [48,49,52,55,56]. For AerMet™100 and Ferrium™M54, respectively, σ_{YS} is 1725 MPa and 1720 MPa and σ_{UTS} is 1965 MPa and 2020 MPa from tensile testing; Ramberg-Osgood constants are n = 13 and 14, α = 1.0, E = 194 and 198 GPa, $\sigma_o = \sigma_{YSc}$ = 1985 MPa and 1951 MPa; and K_{IC} is 130 MPa√m and 126 MPa√m.

The kinetics of HEAC were measured for Monel®K-500, Aer-Met™100, and Ferrium™M54 using precracked fracture mechanics specimens stressed under slow-rising K_I while immersed in an aqueous solution of 0.6 M NaCl and as a function of E_{APP}, as detailed elsewhere [5,46–49]. The da/dt versus K_I results for each alloy are typical of HEAC in high strength metals [7]. Two material properties characterize these data; specifically, the K_{TH} for the onset of resolvable crack propagation under slow-rising K_I, which rapidly accelerates in Stage I then transitions in Stage II to K-independent growth at a plateau level (da/dt$_{II}$) due to chemical reaction or mass transport limitation [10]. The measured E_{APP} dependencies of K_{TH} and da/dt$_{II}$ (taken at a fixed K_I of 40–50 MPa√m within Stage II) are used to assess the predictions of HEAC models that incorporate either MSGP or PSGP. All potentials are expressed with respect to

the saturated calomel reference electrode, SCE.

4. Modeling procedure

4.1. Hydrogen assisted-cracking modeling

K_{TH} is modeled following the approach by Gerberich et al. that yielded [25]:

$$K_{TH} = \frac{1}{\beta'} \exp \frac{(k_{IG} - \alpha C_{H\sigma})^2}{\alpha'' \sigma_{YS}} \tag{1}$$

The β' and α'' constants, 0.2 (MPa$\sqrt{m}$)$^{-1}$ and 0.0002 MPa m, respectively, are determined from numerical analysis of computer simulation results for an assumed configuration of dislocation shielding of the crack tip [24,58], and $C_{H\sigma}$ is defined below. The α (MPa$\sqrt{m}$ per atom fraction H) is a weighting factor, which governs H-lowering of the Griffith toughness (k_{IG}, MPa$\sqrt{m}$), or the reversible work of fracture related to surface energy (γ_S) through $k_{IG}^2 = 2\gamma_S E/(1 - \nu^2)$. The β' and α'' capture the impact of plasticity (plastic work of fracture) on this γ_S-based description. For the cases investigated, H diffusion from the crack tip into the FPZ likely governs the Stage II da/dt$_{II}$, modeled as [49,59,60]:

$$\left(\frac{da}{dt}\right)_{II} = \frac{4D_{H-EFF}}{x_{crit}} \left\{ erf^{-1}\left(1 - \frac{C_{H\sigma - crit}}{C_{H\sigma}}\right) \right\}^2 \tag{2}$$

where x_{crit} is the critical distance ahead of the crack tip where H cracking nucleates leading to an increment of discontinuous crack advance. $C_{H\sigma - crit}$ is the critical concentration of H necessary for H decohesion at x_{crit} and an inverse function of local tensile stress [8,61].

Consistent with the derivations of (1) and (2), $C_{H\sigma}$ must be the crack tip σ_H-enhanced concentration of mobile H in equilibrium with the crack tip overpotential for H production (η_H) and proximate to the interfacial-H crack path within the FPZ. Since σ_H depends on distance ahead of the tip, $C_{H\sigma}$ varies with location, and is evaluated at x_{crit} for use in (1) and (2). $C_{H\sigma}$ is derived as follows. The diffusible (or mobile) H concentration, C_{H-Diff}, is the sum of the normal-interstitial-lattice H (C_L) and reversibly trapped H (C_{RT}) for a single trap site, with C_{RT} in local equilibrium with C_L and described using Fermi-Dirac statics [28]. C_L and C_{RT} are of the same order for face-centered cubic Monel®K-500 [51], but the reversibly trapped H concentration in body-centered martensitic steel is of orders of magnitude higher than C_L [52]. σ_H increases C_L to $C_{L\sigma}$ due to lattice dilation [29], thus enhancing C_{RT} in equilibrium with $C_{L\sigma}$ to yield $C_{H\sigma}$ [46]:

$$C_{H\sigma} = \left[C_L \frac{(1 - C_{L\sigma})}{(1 - C_L)} exp\left(\frac{\sigma_H V_H}{RT}\right)\right] \left[1 + \frac{(1 - C_{RT})}{(1 - C_L)} exp\left(\frac{E_B}{RT}\right)\right] \tag{3}$$

where V_H is the partial molar volume of H in the metal lattice, E_B is the binding energy of H to the dominant-reversible trap site adjacent to the crack path, T is temperature, and R is the gas constant. For H dissolved in the ultra-high strength steels and Ni-Cu superalloy in NaCl solution, C_L and C_{RT} are less than 0.001 atom fraction H, to justify that $(1 - C_L)$ and $(1 - C_{RT})$ equal 1. E_B for H in Monel®K-500 and AerMet™100 is 10 kJ/mol for H trapping at Ni$_3$(Al,Ti) or (Cr,Mo)$_2$C, respectively [51,52]. Therefore, the E_B term in (3) is much greater than 1 and:

$$C_{H\sigma} = \left[(1 - C_{L\sigma}) exp\left(\frac{\sigma_H V_H}{RT}\right)\right] \left[C_L exp\left(\frac{E_B}{RT}\right)\right] \tag{4}$$

The second-bracketed exponential term in (4) is C_{RT}, which essentially equals experimentally measurable C_{H-Diff} and is elevated by σ_H through the first-bracketed term. The $(1-C_{L\sigma})$ often equals 1 since C_L is less than 0.001 wppm and $C_{L\sigma}$ is typically much less than 1.

Diffusible H concentration, unique to the occluded crack tip, must be determined to establish $C_{H\sigma}$ for K_{TH} and da/dt$_{II}$ modeling in (1), (2) and (4). Measurements of artificial crevice pH and potential, coupled with a geometric model that scales crevice behavior to a tight crack, yielded the following relationship between E_{APP}, and crack tip H solubility (C_{H-Diff}) for Monel®K-500 in aqueous chloride [46].

$$C_{H-Diff}(wppm) = -52.5 - 68.7E_{APP}(V_{SCE}) \tag{5}$$

This result is relevant to HEAC in Monel®K-500 with: (a) E_{APP} less than −0.575 V, below the open circuit potential (OCP, about −0.225 V) and (b) 10 cm < ξ < 60 cm, where ξ is the ratio of crack length squared to the average of crack mouth and blunt-tip openings. For AerMet™100 in 0.6 M NaCl at E_{APP} below −0.750 V, the upper and lower bounds on crack tip H solubility are identical, and given by [50]:

$$C_{H-Diff}(wppm) = 19.125E_{APP}^3 + 78.568E_{APP}^2 + 80.026E_{APP}$$
$$+ 24.560 \, (V_{SCE}) \tag{6}$$

for an HEAC-relevant ξ of 15−20 cm (increasing ξ from 10 to 1000 cm results in at most a 10% increase in C_{H-Diff}). For E_{APP} between −0.750 V and −0.480 V, compared to the OCP of about −0.525 V, crack tip C_{H-Diff} is less certain [50]. For example, C_{H-Diff} increases from 1.7 to 2.8 wppm as ξ rises from 10 to 1000 cm, with the latter typical of low K_I (10−20 MPa$\sqrt{m}$) and restricted crack opening compared to classical blunting [23]. Moreover, H solubility is reduced to nearly 0 with increasing crack surface passivation [50]. Given these complications and limited data, for E_{APP} above −0.750 V, crack tip H solubility for the two steels is given by (6) as the lower bound and the following upper bound [50]:

$$C_{H-Diff}(wppm) = -739.24E_{APP}^5 - 3121.1E_{APP}^4 - 5147.1E_{APP}^3$$
$$- 4099.2E_{APP}^2 - 1563.8E_{APP} - 225.77 \, (V_{SCE}) \tag{7}$$

The applied potential dependence of K_{TH} is predicted by relating E_{APP} to $C_{H\sigma}$, using (5) for Monel®K-500 or (6) and (7) for the steels in (4), with the relevant σ_H from SGP FEA; then fitting the single-unknown parameter, α, in (1) to K_{TH} measured for any E_{APP}. A similar procedure is employed to predict the E_{APP} dependence of da/dt$_{II}$ using (2), with measured D_{H-Eff} [51,53] and independently determined x_{crit} [7,60]. Critically, da/dt$_{II}$ is predicted without adjustable parameters since $C_{H\sigma}$ appears in (1) and (2). Equating (1) and (2) defines $C_{H\sigma - crit}$ as a function of α from K_{TH} modeling, plus a single-measured K_{TH} and da/dt$_{II}$ at any E_{APP}:

$$C_{H\sigma - crit} = \frac{1}{\alpha}\left(k_{IG} - \sqrt{\alpha'' \sigma_{YS} \ln(K_{TH}\beta')}\right)$$
$$\times \left[1 - erf\left(\sqrt{\frac{\left(\frac{da}{dt}\right)_{II} \cdot x_{crit}}{4D_H}}\right)\right] \tag{8}$$

$C_{H\sigma - crit}$ from (8) and $C_{H\sigma}$ from (4) must be evaluated at the same K_I; however, any value can be used since $C_{H\sigma - crit}/C_{H\sigma}$ is a constant independent of σ_H and the associated K_I.
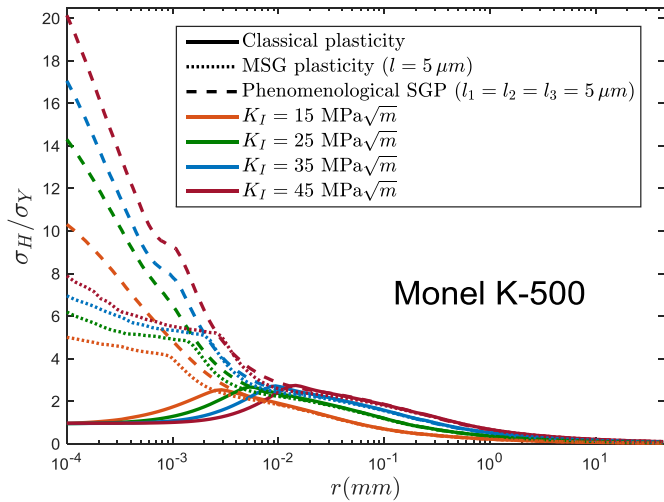
Fig. 1. FEA calculated σ_H/σ_Y versus distance ahead of the blunted crack tip, r, for the range of K_I used in HEAC experiments with Monel®K-500. Formulations include: MSGP ($l_{ref} = 5$ μm), PSGP ($l_{ref} = l_1 = l_2 = l_3 = 5$ μm), and conventional plasticity. σ_Y in the flow rule for FEA [38] is equated to the measured tensile σ_{YS}, and the associated stress-strain relationship is essentially the same as the Ramberg-Osgood fit for Monel®K-500.

4.2. Strain gradient plasticity modeling

PSGP [31] and MSGP models [34] were incorporated in an FEA of crack tip stress, as detailed elsewhere [37,38]. In the PSGP generalization of J2 flow theory [38], hardening due to the plastic strain gradient is incrementally captured through the generalized plastic strain rate ($\dot{E}_P$), formulated as a function of the conventional plastic strain rate ($\dot{\varepsilon}^p$), three unique non-negative invariants (I_i) of $\dot{\varepsilon}^p$, and three material lengths, l_i:

$$\dot{E}_P = \sqrt{\dot{\varepsilon}^{p2} + l_1^2 I_1 + l_1^2 I_2 + l_1^2 I_3} \tag{9}$$

The MSGP formulation is based on the Taylor relationship between flow strength (σ_{flow}) and dislocation density, given by the sum of statistically stored (ρ_S) and geometrically necessary (ρ_G) dislocation densities [33,34]. The GND density is related to the effective plastic strain (ε^p) gradient (η^p) through the Nye-factor ($\bar{r}$) and Burger's vector (b):

$$\rho_G = \bar{r} \frac{\eta^p}{b} \tag{10}$$

These MSGP relationships predict flow strength as a function of ε^p, η^p, a single length parameter (l) and a reference stress (σ_{ref}) determined from the material flow rule [31,37]:

$$\sigma_{flow} = \sigma_{ref} \sqrt{f^2(\varepsilon^p) + l\eta^p} \tag{11}$$

Since the Taylor dislocation model represents an average of dislocation activities, the MSGP theory is only applicable at a scale larger than the average dislocation spacing ($r \geq 100$ nm).

The material-dependent length is a single or multiple coefficient(s), calculated to fit experimental measurements of a size dependent property (e.g., hardness) using a specific SGP theory. Various micro-tests should be conducted to establish the l_i parameter(s); however, this determination is outside the scope of the present work. The observed range of l_i for metals is from 300 nm to 10 μm (e.g., [30,62–64]). Reference lengths ($l = l_{ref}$ in MSGP and $l_1 = l_2 = l_3 = l_{ref}$ in PSGP) of 5 μm for Monel®K-500 and 7 μm for AerMet™100 are adopted. The former is based on micro-bending experiments with pure nickel [30],

while the choice for AerMet™100 rests on nano-indentation tests with a moderate strength steel [64]. A constant l_{ref} is assumed in the PSGP model, as different weighting of individual length parameters has little influence in finite strain crack tip analyses [38]. The influence of length scale is addressed in the Discussion.

Crack tip stress analysis by boundary layer FEA, with PSGP and MSGP in the finite-strain framework, is detailed elsewhere [37,38]. K_I quantifies the applied load, assuming plane strain and small-scale yielding. A refined mesh is used near the tip, where the length of the smallest element is 5 nm. The cracked body is discretized by 6400 quadrilateral quadratic elements and the starting blunt-tip radius is 10^{-5}-times the outer radius of the field [23].
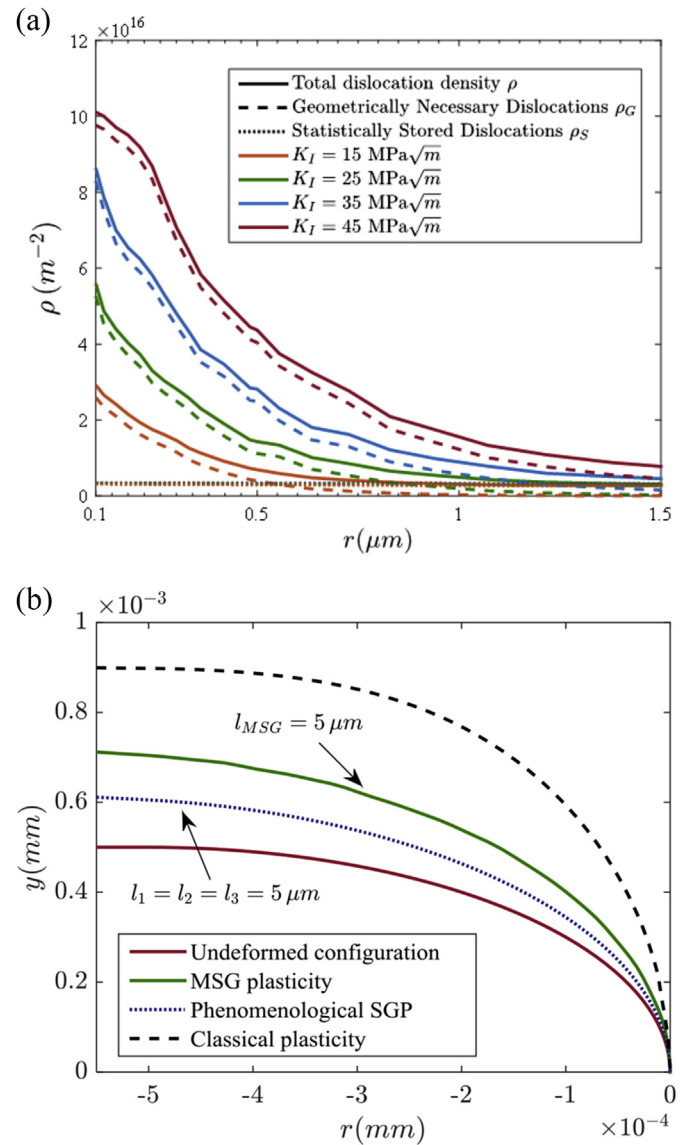

Fig. 2. SGP-FEA calculations for Monel®K-500 with $l_{ref} = 5$ μm: (a) MSGP results showing ρ_S and ρ_G versus r for the range of K_I used in the HEAC experiments, and (b) MSGP and PSGP predictions of blunt-crack opening shape for $K_I = 15$ MPa$\sqrt{m}$ compared to the profile from classical plasticity.

5. Results

5.1. Monel®K-500

The crack tip hydrostatic stress distribution is computed for several applied K_I in the range where HEAC occurred in Monel®K-500. Fig. 1 shows normalized σ_H/σ_Y versus distance from the crack tip, r, for three cases: MSGP (with $l_{ref} = 5$ μm), PSGP (with $l_1 = l_2 = l_3 = l_{ref} = 5$ μm), and classical von Mises plasticity. All finite-strain, blunt-crack predictions agree beyond the location of maximum stress in the classical analysis, but significant differences arise closer to the crack tip. These findings are consistent with SGP results for a low strength-high work hardening alloy [38]. Specifically, for MSGP and PSGP compared to conventional plasticity: (1) crack tip stresses are substantially elevated, (2) a stress maximum is not evident, and (3) the stress distribution rises with increasing K_I. For the length(s) used, σ_H levels from the 3-parameter PSGP model are higher than those predicted with MSGP. For each model, the maximum distance of 2.5–12 μm ahead of the crack tip where GNDs significantly influence the stress distribution suggests that SGP plays an important role in HEAC. Fig. 2 shows MSGP-predicted GND density from (10) and the reduced crack tip profile in the opening (y) direction for each SGP formulation. The ρ_S (Fig. 2a) is determined from the uniaxial stress-strain curve [38], and the very high and localized GND density from SGP is apparent for each K_I level. Crack tip opening (Fig. 2b) is reduced by hardening from this high ρ_G.

For HEAC modeling, crack tip σ_H is averaged over two distances, 0.1 μm $< r < 1$ μm and 0.1 μm $< r < 2$ μm, as justified in the Discussion, and values are given in Table 1 including results for a low strength alloy [38]. K_{TH} from (1) is predicted versus E_{APP} for the PSGP and MSGP-model values of σ_H/σ_Y (the average of the 1 μm and 2 μm intervals of r, Table 1) using $C_{H\sigma}$ from (4) and (5). Model results in Fig. 3a are compared to experimental data for Monel®K-500 in 0.6 M NaCl solution [46,47]. The 3-replicate measurements of K_{TH} at E_{APP} of -1.000 V are used to determine α, which equals 6.36 MPa$\sqrt{m}$ (at frac H)$^{-1}$ for PSGP-based σ_H (8.1σ_Y) and 37.59 MPa$\sqrt{m}$ (at frac H)$^{-1}$ for MSGP σ_H (4.7σ_Y). The remaining constants in (1) were justified, including k_{IG} of 0.880 MPa$\sqrt{m}$ from γ_S for Ni [46]. Since C_L is 0.1 to 15 wppm for Monel®K-500 in NaCl solution at E_{APP} from -0.75 to -1.20 V [46], $C_{L\sigma}$ is 0.0005 to 0.007 atom fraction for the highest crack tip σ_H in Table 1 and $(1 - C_{L\sigma})$ is essentially 1.0 in (4). The PSGP and MSGP-based predictions of K_{TH} similarly agree with measured values over a range of E_{APP}; only α rises as crack tip σ_H falls. Each α from the Fig. 3a fit is used to calculate a $C_{H\sigma-crit}$ through (8) with K_{TH} and da/dt$_{II}$ measured at E_{APP} of -1.000 V. The da/dt$_{II}$ is then calculated from (2) and the results are given in Fig. 3b. The PSGP and MSGP predictions of da/dt$_{II}$ are essentially identical, and agree with measured da/dt$_{II}$ at a single K_I of 50 MPa$\sqrt{m}$ [46,47].[1]

5.2. AerMet™ 100 and Ferrium™ M54

The crack tip hydrostatic stress distribution is computed for several K_I relevant to HEAC of AerMet™100 and Ferrium™M54. Fig. 4 shows σ_H/σ_Y versus r for MSGP ($l_{ref} = 7$ μm), PSGP ($l_{ref} = l_1 = l_2 = l_3 = 7$ μm), and classical plasticity. Stresses are given in Table 1, and show the same behavior as Monel®K-500 (Fig. 1) and a low strength alloy [38].

K_{TH} versus E_{APP} is predicted from (1) and (4) using crack tip H solubility from either the upper bound given by (6) and (7) or the lower-bound in (6); the results are presented in Figs. 5 and 6. Parts (a) and (b) of each figure show the PSGP and MSGP results, respectively. The three levels of averaged σ_H/σ_Y (Table 1) correspond to K_I of 10 MPa$\sqrt{m}$, 20 MPa$\sqrt{m}$, and 40 MPa$\sqrt{m}$. The k_{IG} is 1.145 MPa$\sqrt{m}$ for each steel, and the α'' and β' are identical to those used for Monel®K-500 [47] and steel [25]. Griffith toughness was estimated based on maximum modeled γ_S for a {100} surface of Fe (3.09 J/m² [65]) and Poison's ratio of 0.29. This k_{IG} yielded a H-free K_{IC} of 224 MPa$\sqrt{m}$ through (1), which is reasonably higher than the intervening microvoid based K_{IC} (130 MPa$\sqrt{m}$). However, the precise Griffith toughness for a HEDE-sensitive martensite block or packet interface in AerMet™100 and Ferrium™M54 is not known [48]. Each SGP prediction is given by a solid plus dashed curve, and compared to experimental measurements of K_{TH} [50,51].[2] For each case examined, an average α is calculated using the six experimental values of K_{TH} at E_{APP} of -0.900 V and lower. This regime was selected because H solubility is well known through (6), HEAC is severe (measured K_{TH} varied between 9 MPa$\sqrt{m}$ and 14 MPa$\sqrt{m}$ with an average of 10.5 MPa$\sqrt{m}$), HEAC is reproducible (3 replicated values are essentially equal for Ferrium™M54 at E_{APP} of -1.000 V), and HEAC is fully transgranular associated with martensite interface decohesion [48]. Average-calculated α values are given in Figs. 5 and 6. The dashed curves show the regime of E_{APP} where the K_{TH} model from (1) is expected to under-predict true K_{TH} for HEAC, as justified in the Discussion.

The E_{APP} dependence of da/dt$_{II}$ is predicted without any adjustable constants using independently established D_{H-EFF} [53] and x_{crit} [60]; results are shown for upper bound (Fig. 7) and lower bound (Fig. 8) $C_{H,Diff}$. PSGP ($\sigma_H = 7.2\sigma_Y$, solid line) and MSGP ($\sigma_H = 5.3\sigma_Y$, dashed line) predictions are shown in each plot, and compared to da/dt$_{II}$ measured at a K_I of 40 MPa$\sqrt{m}$ [48,49]. Each $C_{H\sigma-crit}$ is calculated through (8), using the appropriate α from the Figs. 5 and 6 fits at K_I of 40 MPa$\sqrt{m}$, coupled with the average K_{TH} and average da/dt$_{II}$ measured at E_{APP} of -1.000 V. Downward arrows represent experiments where K_{TH} exceeded 40 MPa$\sqrt{m}$, and HEAC was not resolved; all other data are associated with transgranular HEAC [48,49]. The predictions of the SGP-HEAC model in Figs. 5–8 effectively capture the complex dependencies of K_{TH} and da/dt$_{II}$ over a wide range of E_{APP}.

6. Discussion

6.1. SGP impact on hydrogen cracking

Strain gradient plasticity (SGP) enhanced large-strain finite element analysis (FEA) results reveal a profound influence of geometrically necessary dislocation (GND) density on crack tip mechanics for technologically important alloys. Simulation results in Figs. 1, 2 and 4 establish the following effects of mechanism-based (MSGP) and phenomenological (PSGP) strain gradient plasticity compared to classical plasticity analysis of a blunt crack tip.

- Crack tip stresses are substantially elevated, and crack opening is reduced, due to hardening from high-GND density. This reduced CTOD is strictly a continuum mechanics effect, which is

---

[1] Filled points in Fig. 3 represent 100% intergranular HEAC, while open points with upward arrows show those E_{APP} that did not produce intergranular HEAC for the highest-applied K_I [47]. The two points at E_{APP} (■) of -0.900 and -0.800 V were associated with intergranular HEAC attributed to specimen-to-specimen variability in grain boundary-S segregation. This behavior was captured by higher α, lower k_{IG}, and lower $C_{H\sigma-crit}$ than used for the majority of K_{TH} and da/dt$_{II}$ measurements in Fig. 3 [47]. These parameter changes are consistent with grain boundary weakening due to S interaction with H.

[2] The largest C_{H-Diff} is 6 wppm, and C_L is about 0.06 wppm, at the most cathodic E_{APP} examined. As such, $C_{L\sigma}$ is 0.01 atom fraction H for the highest σ_H/σ_Y of 7.2 and the calculations in Fig. 5 equate $(1-C_{L\sigma})$ in (4) to 1.

Table 1
Large strain FEA predictions of σ_H/σ_Y, at $r = 1$ or 2 μm ahead of the blunted crack tip for conventional plasticity, and averaged between the blunted crack tip and $r = 1$ or 2 μm for two SGP formulations with $l_{ref} = 5$ μm for Monel®K-500 and $l_{ref} = 7$ μm for AerMet™100.

σ_H/σ_Y	K_I (MPa$\sqrt{m}$)	Classical ($r = 1, 2$ μm)	MSGP ($r = 1, 2$ μm)	PSGP ($r = 1, 2$ μm)	Elastic singular ($r = 0.25, 1$ μm)
AerMet™100 (Fig. 4)	10	1.8, 1.7	2.2, 2.0	2.8, 2.5	4.1, 2.1
	20	1.4, 1.6	3.4, 3.1	4.6, 4.1	8.2, 4.2
	40	0.8, 1.1	5.5, 5.1	7.6, 6.8	16.4, 8.4
	80	0.5, 0.8	8.6, 8.1	14.0, 13.2	32.8, 16.8
Monel®K-500 (Fig. 1)	17.3	1.5, 1.8	4.8, 4.6	8.6, 7.7	15.9, 7.9
	50	1.0, 1.1	7.1, 6.7	16.8, 16.5	45.9, 22.8
Low strength [38]	22.4	2.8, 3.6	10.4, 9.1	21.0, 16.0	39.8, 19.9

not related to H-plasticity interaction that could impact the local slip mode, hardening/softening, or crack path through the microstructure [9].

- σ_H levels from the 3-parameter PSGP model are substantially higher than those predicted by the MSGP formulation.
- The maximum in tensile stress with increasing distance is shifted to within 100 nm or less from the blunted crack tip by SGP hardening.

- The crack tip stress distribution from SGP rises and broadens with increasing K_I.
- The magnitude of SGP-elevated σ_H/σ_Y decreases with increasing alloy strength and the maximum crack tip σ_H is essentially constant (6300 MPa or ~0.035E).[3]
- GND density and σ_H are elevated over 1–20 μm ahead of the crack tip, suggesting that SGP impacts hydrogen (H) cracking in the fracture process zone (FPZ).

It is imperative to account for the strain gradient in modeling of hydrogen environment (HEAC) and internal hydrogen (IHAC) assisted cracking over a wide range of alloy strengths.

6.2. Fracture process zone definition

A critical distance, x_{crit}, from the crack tip surface to FPZ sites of H damage formation, is required to define crack tip σ_H to calculate $C_{H\sigma}$ through (4) and da/dt_{II} in (2). Classical plasticity equates this distance to the location of maximum stress [13–23], evident in Figs. 1 and 4. This classical x_{crit} is 6–13 μm for Monel®K-500 at K_I of 25–45 MPa$\sqrt{m}$ and 5–10 μm for AerMet™100 at K_I of 30–50 MPa$\sqrt{m}$. In contrast empirical analysis suggests that x_{crit} is 1 μm for alloys of different strengths and wide ranging K_I [60]. A micro-meter-scale critical distance is consistent with the SGP predictions in Figs. 1 and 4.

The SGP results suggest that x_{crit} is the location of the highest probability of H-assisted crack formation, governed by interaction of decreasing σ_H (and decreasing $C_{H\sigma}$) with the increasing number of defect-based initiation sites within the FPZ; each with increasing r. The details of H-crack formation are not sufficiently defined to quantify x_{crit}, following the approach used to model cleavage [67]. Electron microscopy suggests that hydrogen-enhanced localized plasticity (HELP) concentrates stress to promote interface hydrogen-enhanced decohesion (HEDE) [9]. Speculatively, the number of crack formation sites scales with ρ_G and interacts with $C_{H\sigma}$ to establish x_{crit}. For Monel®K-500, GND density from MSGP is above ρ_S for r up to 0.5 μm at K_I of 15 MPa$\sqrt{m}$ and 2.2 μm at 45 MPa$\sqrt{m}$ (Fig. 2). Similar behavior is suggested for AerMet™100, since σ_H is elevated by MSGP for r of up to 1–6 μm for HEAC relevant K_I of 10 MPa$\sqrt{m}$ to 40 MPa$\sqrt{m}$ (Fig. 4).

Reversible H trapping at precipitate-matrix interfaces is extensive within an μm-scale FPZ for both alloys studied. The small size (1–5 nm) and large number density of (Ni$_3$(Al,Ti) spheres and (Cr,Mo)$_2$C needles results in a mean-free path between precipitate surfaces of 25–40 nm for the steels and 60–75 nm for Monel®K-500. Thermal desorption analysis affirmed that up to 1.5×10^8 H atoms (32 wppm) are trapped by monolayer coverage on all (Cr,Mo)$_2$C -surface sites in 1 μm^3 of AerMet™100 for a single H
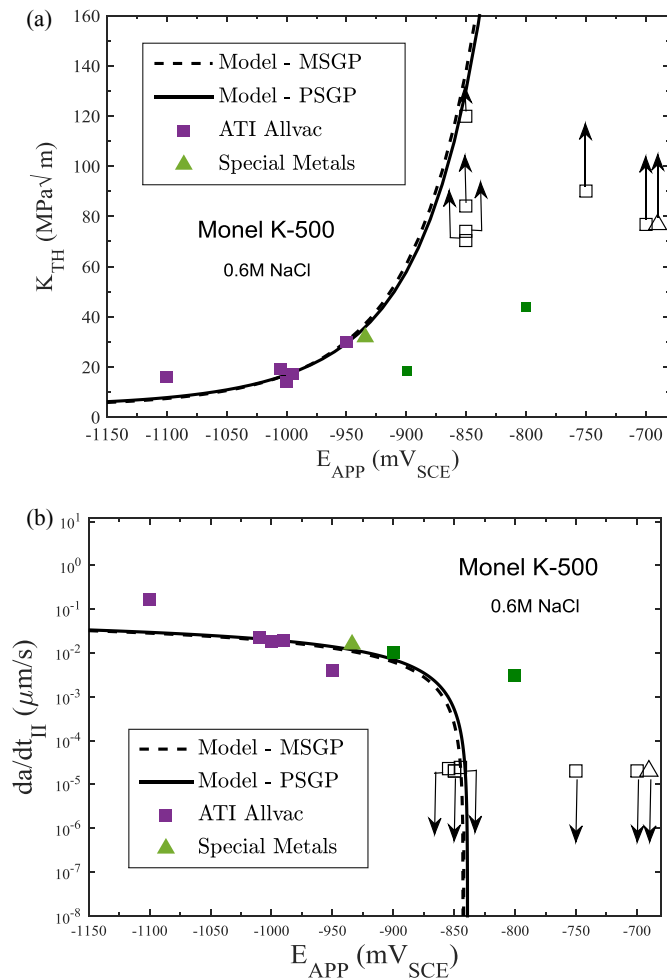
Fig. 3. H-decohesion based predictions for Monel®K-500 in 0.6 M NaCl solution, calibrated by adjusting α in (1) to fit the average of replicate experimental measurements of K_{TH} at $E_{APP} = -1.000$ V for σ_H determined by PSGP (solid line, $\sigma_H = 8.15\sigma_Y$, $\alpha = 6.36$ MPa$\sqrt{m}$ (at frac H)$^{-1}$ and $C_{H\sigma-crit} = 407$ wppm), as well as MSGP (dashed line, $\sigma_H = 4.7\sigma_Y$, $\alpha = 37.59$ MPa$\sqrt{m}$ (at frac H)$^{-1}$ and $C_{H\sigma-crit} = 68$ wppm), each with $l_{ref} = 5$ μm; (a) K_{TH} versus E_{APP} and (b) da/dt_{II} versus E_{APP}. Other parameters are $k_{IG} = 0.880$ MPa$\sqrt{m}$ [46], $D_{H-EFF} = 1\cdot10^{-10}$ cm^2/s [50], and $x_{crit} = 1$ μm [55].

[3] Regression analysis of the PSGP simulation results (at $K_I = 20$ MPa$\sqrt{m}$, averaged over the two intervals of r for the alloys in Table 1) yields $\sigma_H/\sigma_{YS} = 6300/\sigma_Y$ (in MPa).
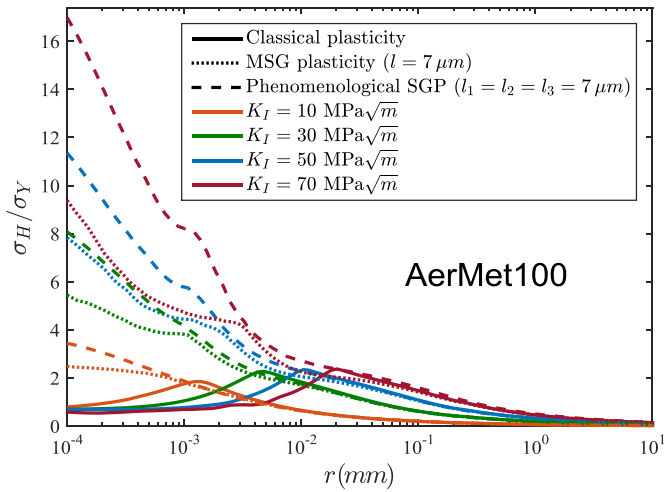
Fig. 4. FEA calculated σ_H/σ_Y versus distance ahead of the blunted crack tip, r, for the range of K_I used in the HEAC experiments with AerMet™ 100. Formulations include: MSGP ($l_{ref} = 7$ μm), PSGP ($l_{ref} = l_1 = l_2 = l_3 = 7$ μm) and conventional plasticity. The σ_Y in the flow rule for FEA [38] is equated to measured tensile σ_{YS} of 1725 MPa and the associated stress-strain relationship is essentially the same as the Ramberg-Osgood fit for AerMet™100 corrected for the difference in tension versus compression for martensitic steels [66].

overpotential [52]. Additionally, C_L is a significant fraction (about 0.5) of $C_{H\text{-Diff}}$ for the fcc superalloy and interstitial jump distance is of order 1 nm [51]. It follows that (1) through (4) provide a physically reasonable description of HEAC for the alloys considered.

Measurements that affirm x_{crit} are not widely available. Micrometer spaced makings attributed to H cracking were convincingly demonstrated for oriented-single crystal Fe-Si, and a martensitic steel [25,68]. These results not-with-standing, the small x_{crit} challenges measurements using SEM, acoustic emission, electrical potential, or electrochemical current. Markings associated with x_{crit} were not observed by SEM analysis of Monel®K-500, AerMet™100, or Ferrium™M54 for the cases modeled [46,48,49]. The martensitic microstructure of these steels, which constitutes the transgranular HEAC path [48,49], obscures crack advance markings, and a blunting-based feature may not occur in the short time (1–1000 s from Figs. 7 and 8) between crack advance in a creep resistant alloy. For lower strength Monel®K-500, intergranular HEAC features are more likely to show markings, but these can be either crack wake slip steps (not relevant to crack advance) or due to discontinuous advance over x_{crit}. Work is required to characterize the sites of H damage within the crack tip FPZ [69].

6.3. Crack growth rate modeling

To model HEAC, x_{crit} was taken as 1.0 μm as a proxy for statistical analysis, and the average of the two stress levels in Table 1 was used for each SGP model, alloy, and K_I. Figs. 7 and 8 show that measured and model predicted da/dt$_{II}$ agree precisely for AerMet™100 at the most cathodic E_{APP} examined. Here, for the high-PSGP stress level, severe HEAC is diffusion controlled and the combination of independently measured $D_{H\text{-EFF}}$ and x_{crit} of 1.0 μm predicts measured da/dt$_{II}$ through (2). Reasonable agreement is observed for Monel®K-500 at the most cathodic E_{APP} below −1.000 V (Fig. 3b); however, x_{crit} would have to equal 0.35 μm for precise-model agreement with the single-highest da/dt$_{II}$. SGP modeling justifies an x_{crit} of order 1 μm for HEAC, at least within the accuracy and relevance of measured $D_{H\text{-EFF}}$ [70,71].

The distributions of crack tip σ_H and ρ_G from SGP-FEA simulation can improve the accuracy of H diffusion models pertinent to
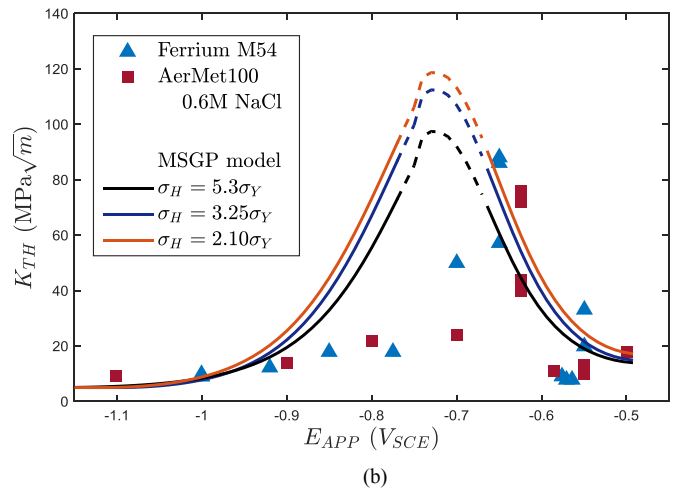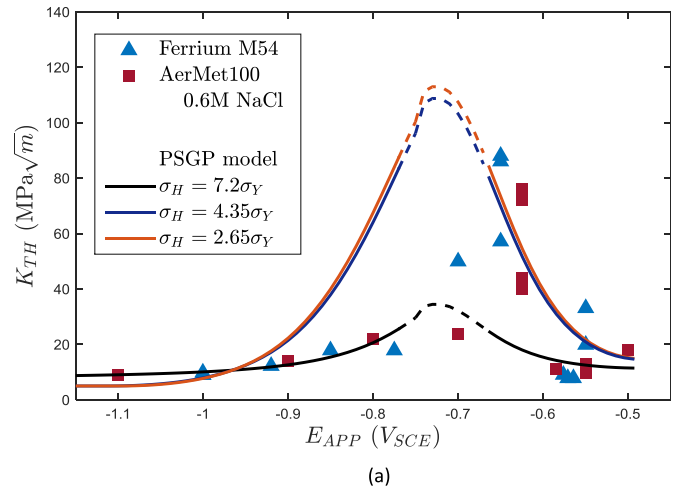

(a)

(b)

Fig. 5. Predicted K_{TH} versus E_{APP} from (1) for AerMet™100 and Ferrium™ M54 in 0.6 M NaCl, calculated using upper bound $C_{H,Diff}$ from (6) and (7), and calibrated by averaging α by fitting to six K_{TH} values measured at $E_{APP} \leq -0.9$ V; $k_{IG} = 1.145$ MPa$\sqrt{m}$ for each steel. The σ_H is estimated from either: (a) PSGP or (b) MSGP FEA at K of 10 MPa$\sqrt{m}$ (orange line: (a) $\bar{\alpha} = 81.37$ MPa$\sqrt{m}$ (at frac H)$^{-1}$ and (b) $\bar{\alpha} = 161.81$ MPa$\sqrt{m}$ (at frac H)$^{-1}$), 20 MPa$\sqrt{m}$ (blue line: (a) $\bar{\alpha} = 8.18$ MPa$\sqrt{m}$ (at frac H)$^{-1}$ and (b) $\bar{\alpha} = 35.64$ MPa$\sqrt{m}$ (at frac H)$^{-1}$) and 40 MPa$\sqrt{m}$ (black line: (a) $\bar{\alpha} = 0.76$ MPa$\sqrt{m}$ (at frac H)$^{-1}$ and (b) $\bar{\alpha} = 2.65$ MPa$\sqrt{m}$ (at frac H)$^{-1}$). The σ_H/σ_Y listed on each plot increased as K_I rose from 10 to 20–40 MPa$\sqrt{m}$.

HEAC and IHAC. The da/dt$_{II}$ model in (2) does not include the effects of crack tip stress gradient on H flux and dislocation trapping of H on $D_{H\text{-EFF}}$ (typically from a stress-free H permeation experiment and approximate trapping analysis [70]). Sophisticated models address such complications [20,21,71]; however, these center on blunt-crack σ_H and ρ_S associated with plastic strain from classical plasticity [23]. In these models, the maximum crack tip σ_H provides a positive stress gradient ahead of the crack tip, which increases the flux of H from the tip surface to x_{crit} [19–21,59]. However, σ_H monotonically declines with increasing r due to SGP, at least for distances greater than 100 nm (Figs. 1 and 4); dσ_H/dr is mildly negative for MSGP and more strongly so for PSGP. The SGP-stress gradient retards H diffusion to x_{crit}. Second, the GND distribution due to SGP (Fig. 2a) provides dislocation sites for reversible-H trapping that reduce $D_{H\text{-EFF}}$. Provided the binding energy of H to GND structure is known, equilibrium trapping theory can estimate
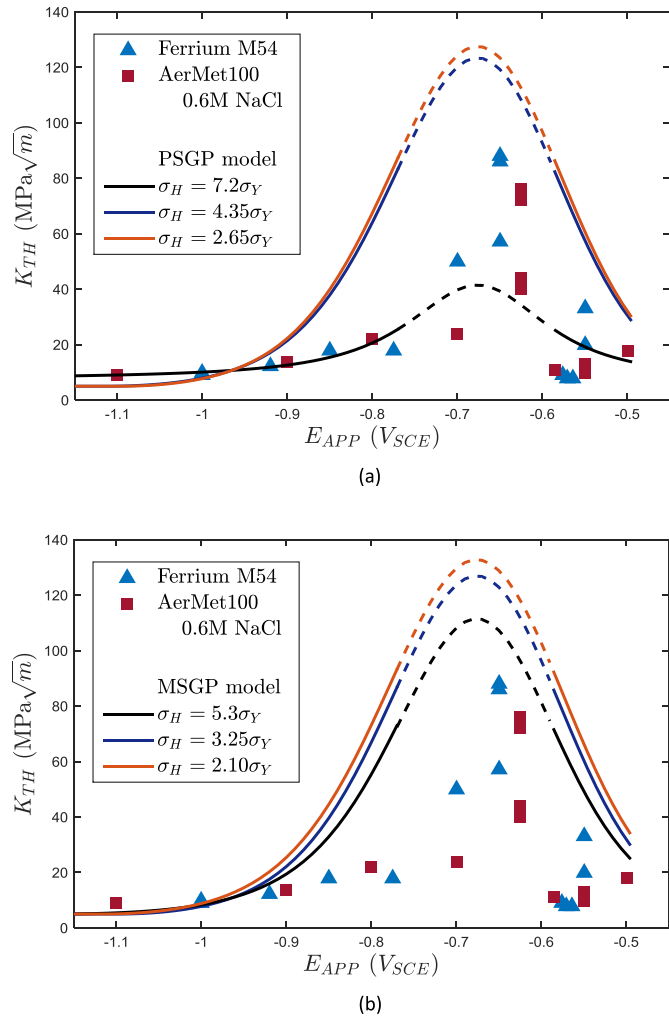
(a)

(b)

Fig. 6. Predicted K_{TH} versus E_{APP} from (1) for AerMet™100 and Ferrium™M54 in 0.6 M NaCl, calculated using lower bound $C_{H,Diff}$ from (6) and calibrated by averaging α from six experimental K_{TH} values measured at $E_{APP} \leq -0.9$ V; $k_{IG} = 1.145$ MPa$\sqrt{m}$ for each steel. The σ_H is estimated from either: (a) PSGP or (b) MSGP FEA at K of 10 MPa$\sqrt{m}$ (orange line: (a) $\overline{\alpha} = 81.37$ MPa$\sqrt{m}$ (at frac H)$^{-1}$ and (b) $\overline{\alpha} = 161.81$ MPa$\sqrt{m}$ (at frac H)$^{-1}$), 20 MPa$\sqrt{m}$ (blue line: (a) $\overline{\alpha} = 8.18$ MPa$\sqrt{m}$ (at frac H)$^{-1}$ and (b) $\overline{\alpha} = 35.64$ MPa$\sqrt{m}$ (at frac H)$^{-1}$) and 40 MPa$\sqrt{m}$ (black line: (a) $\overline{\alpha} = 0.76$ MPa$\sqrt{m}$ (at frac H)$^{-1}$ and (b) $\overline{\alpha} = 2.65$ MPa$\sqrt{m}$ (at frac H)$^{-1}$). The σ_H/σ_Y listed on each plot increased as K_I rose from 10 to 20–40 MPa$\sqrt{m}$.

the effect of dislocation density on the H diffusivity distribution relevant to the FPZ [28,70].

SGP modeling (Table 1) establishes that crack tip tensile stress rises with increasing K_I, which appears to be at odds with K_I independent da/dt in Stage II [7,10]. For example, σ_H rises from $7.2\sigma_{YS}$ to $13.6\sigma_{YS}$ as K_I increases from 40 MPa$\sqrt{m}$ to 80 MPa$\sqrt{m}$ for AerMet™100 (PSGP, Table 1), but da/dt is constant [48,49]. The H-diffusion model in (2) shows that da/dt_{II} depends on $C_{H\sigma-crit}/C_{H\sigma}$; critically, this ratio is independent of K_I since each concentration is amplified by the same exponential dependence on σ_H through (3) and (4).[4] Any K_I can be used; however, a lower K_I somewhat above
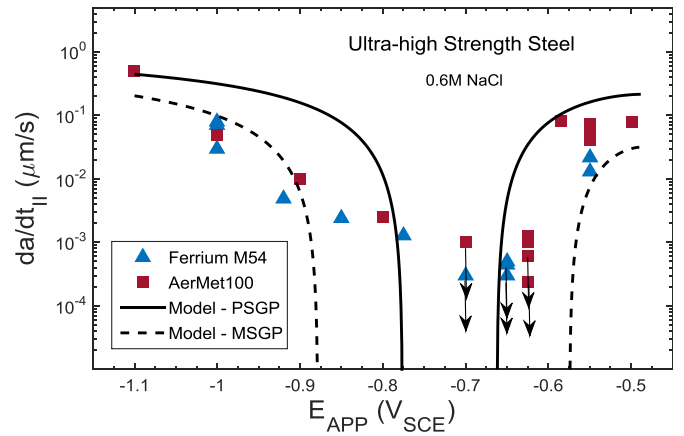
Fig. 7. da/dt_{II} versus E_{APP} predicted from (2) with upper bound $C_{H,Diff}$ from (6) and (7) for AerMet™100 and Ferrium™M54 in 0.6 M NaCl. The σ_H is determined for K of 40 MPa$\sqrt{m}$ using either PSGP (solid line, $C_{H\sigma-crit} = 18,867$ wppm for $\sigma_H/\sigma_Y = 7.2$) or MSGP (dashed line, $C_{H\sigma-crit} = 3,056$ wppm for $\sigma_H/\sigma_Y = 5.3$). Other parameters are $k_{IG} = 1.145$ MPam, $D_{H-EFF} = 1 \cdot 10^{-9}$ cm^2/s [52] and $x_{crit} = 1$ μm [55].

K_{TH} reduces $C_{H\sigma}$. When $C_{H\sigma}$ is large (~0.5–1.0 atom fraction H), stress due to lattice expansion from H in interstitial sites offsets the lattice dilating impact of σ_H [24,72]. This issue is important for ultra-high strength steel, high K_I, and PSGP models (Table 1) where σ_H/σ_{YS} above 9 results in unrealistic values of $C_{H\sigma}$ exceeding 1.0 atom fraction.

6.4. SGP-HEAC model validation

The results of the present investigation affirm the integration of cutting edge SGP-FEA formulations with crack electrochemistry and two HEAC models to predict material-environment properties, specifically K_{TH} and da/dt_{II} as a function of environmental H activity. Models with a single calibration constant are validated over a broad range of applied polarization using precise experimental measurements of these HEAC properties. Excellent agreement is reported for a Ni-Cu superalloy with cathodic E_{APP}. The comparison for two ultra-high strength steels is good, but hindered by crack mechanics and electrochemical uncertainties.
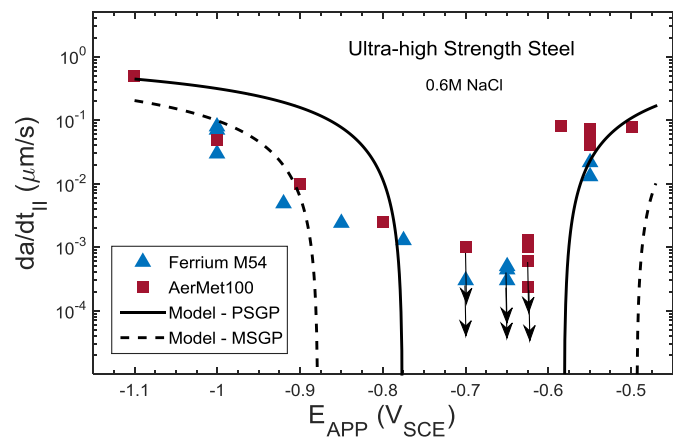

Fig. 8. da/dt_{II} versus E_{APP} predicted from (2) with lower bound $C_{H,Diff}$ from (6) for AerMet™100 and Ferrium™M54 in 0.6 M NaCl. The σ_H is determined for K of 40 MPa$\sqrt{m}$ using either PSGP (solid line, $C_{H\sigma-crit} = 18,867$ wppm for $\sigma_H/\sigma_Y = 7.2$) or MSGP (dashed line, $C_{H\sigma-crit} = 3,056$ wppm for $\sigma_H/\sigma_Y = 5.3$). Other parameters are $k_{IG} = 1.145$ MPam, $D_{H-EFF} = 1 \cdot 10^{-9}$ cm^2/s [52] and $x_{crit} = 1$ μm [55].

6.4.1. Monel®K-500

The SGP-based predictions of K_{TH} and da/dt_{II} versus E_{APP} quantitatively agree with experimental measurements for a single lot of Monel®K-500 stressed under slow-rising K_I in 0.6 M NaCl solution with cathodic polarization. Occluded-crack electrochemistry was previously detailed [46,51], as was specimen variability due to grain boundary S segregation (Footnote 2) [46,47]. The one-length-parameter MSGP and three-term PSGP models of crack tip σ_H/σ_{YS} similarly predict the applied potential dependence of K_{TH} that agrees with experimental measurements over a range of cathodic E_{APP} (Fig. 3a). Moreover, $C_{H\sigma\text{-crit}}$ calculated from K_{TH}-calibrated α predicts the E_{APP} dependence of da/dt_{II} that agrees equally well with experimental measurements for both MSGP and PSGP (Fig. 3b). Since only α was calibrated at a single-low E_{APP} (-1.000 V) to model K_{TH}, with all other parameters in (2) (α'', β', and k_{IG}) justified [47], and since no adjustable parameters were used to predict da/dt_{II}, the models represented by (1) and (2) are validated and consistent. The impact is clear; the wide-range dependence of HEAC properties on cathodic polarization is predicted with α calibrated at a single E_{APP}. This prediction includes an accurate value of the technologically critical potential, above which HEAC is eliminated.

Considering classical plasticity for K_{TH} of 17.3 MPa$\sqrt{m}$, σ_H/σ_{YS} is 1.5 at 1 μm ahead of the crack tip and 2.6 at the location ($r = 3$ μm) of the maximum stress (Fig. 1). Predictions of K_{TH} versus E_{APP} using either of these σ_H levels agree with experimental values with α of 209.5 MPa$\sqrt{m}$ (atom frac H)$^{-1}$ for $\sigma_H/\sigma_{YS} = 1.5$ giving $C_{H\sigma\text{-crit}}$ of 12.3 wppm through (8) or α of 116.0 MPa$\sqrt{m}$ (atom frac H)$^{-1}$ for $\sigma_H/\sigma_{YS} = 2.6$ giving $C_{H\sigma\text{-crit}}$ of 22.2 wppm. The K_{TH} versus E_{APP} agreement form these classical plasticity predictions is essentially identical to the SGP-based results in Fig. 3a. However, the stress maximum in the classical model suggests that x_{crit} is 3–14 μm, for K_I between 15 and 45 MPa$\sqrt{m}$, rather than 1 μm justified by SGP. As such, classical plasticity-based predictions of da/dt_{II} are reduced by 3-fold to 14-fold at any E_{APP} compared to the SGP curves in Fig. 3b where $x_{crit} = 1$ μm. While K_{TH} modeling does not distinguish the most accurate crack tip stress field, the SGP models provide more accurate predictions of da/dt_{II} compared to classical plasticity. This comparison supports the relevance of crack tip stress elevation due to GNDs.

6.4.2. AerMet™100 and Ferrium™M54

SGP-HEAC model predictions of K_{TH} and da/dt_{II} versus E_{APP} agree with measurements for AerMet™100 and Ferrium™M54 stressed under slow-rising K_I in 0.6 M NaCl solution, as shown in Figs. 5–8. First, absolute values of K_{TH} at potentials above -0.600 V are accurately predicted using the single α calibrated at low E_{APP} (Fig. 5). In each regime transgranular HEAC is severe. Agreement is quantitatively strong for the highest level of crack tip stress from the PSGP simulation in Fig. 5a. Second, the window of E_{APP} between -0.600 V and -0.800 V, where K_{TH} rises sharply and da/dt_{II} falls toward zero, is captured, as governed by the minimum in $C_{H\text{-Diff}}$ versus E_{APP} given by (6) and (7). Third, reasonable predictions of da/dt_{II} without adjustable parameters, using $C_{H\sigma\text{-crit}}$ calculated from α, demonstrate the consistency of the HEAC models given by (1) and (2).

Model assessment is demanding for steels given the change in occluded crack chemistry, which accompanies transition from cathodic to anodic polarization through the open circuit potential (OCP) of about -0.525 V. Crack tip $C_{H\text{-Diff}}$ is uncertain for E_{APP} above about -0.750 V owing to limited crack chemistry measurements and the effect of surface passivation [50]. It is only possible to bound $C_{H,Diff}$ using (6) and (7), leading to the upper and lower bound predictions of K_{TH} (Figs. 5 and 6) and da/dt_{II} (Figs. 7 and 8). The best prediction of the E_{APP} dependence of

these HEAC properties likely resides between these bounds. Second, the dashed parts of the predicted curves in Figs. 5 and 6 show the regime of E_{APP} where $C_{H\text{-Diff}}$ is less than 0.8 wppm and should promote mixed transgranular H-cracking and ductile microvoid fracture [73]. These dashed lines should under-predict measured K_{TH} since the HEAC model in (1) does not capture the added cracking resistance associated with ductile growth. Third, K_{TH} and low da/dt are difficult to measure when plasticity at higher K_I gives a false indication of low-rate crack extension from electrical potential measurement [48]. The variability of measured K_{TH} for -0.800 V $< E_{APP} < -0.625$ V is due in part to this limitation. Finally, surface reaction may interact with H diffusion for E_{APP} below about -0.750 V [74]. The da/dt_{II} from the H diffusion model in (2) is an upper bound when surface reaction is slow.

With these considerations, Figs. 5–8 establish that the best agreement between measured and predicted K_{TH} and da/dt_{II} is achieved over a wide range of E_{APP} for PSGP-based σ_H/σ_Y of 7.2. These figures suggest that σ_H as low as $6.0\sigma_Y$ provides similar-good predictions. However, lower crack tip stress levels ($2.1 < \sigma_H/\sigma_Y < 5.3$) provide poor agreement between measured and predicted HEAC properties for either the upper or lower bound H solubilities. For this high σ_H regime, the bounds of crack tip H solubility in (6) and (7) are affirmed, as is evident by comparison of the solid line predictions of da/dt_{II} versus E_{APP} above -0.800 V in Figs. 7 and 8 (speculatively, growth rates for E_{APP} below -0.850 V are lower than the H-diffusion model prediction due to surface reaction rate limitation [74]). The K_{TH} versus E_{APP} predictions are mixed. Upper bound H solubility provides the best-absolute agreement in K_{TH} for E_{APP} above about -0.600 V and below -0.700 V (Fig. 5a), but the lower bound $C_{H\text{-Diff}}$ relationship (Fig. 6a) better captures the range of E_{APP} (-0.770 to -0.585 V) where the dashed line defines the lower bound on the variability in K_{TH} explained by plasticity-microvoid cracking and hindered crack growth resolution. It is likely that specimen to specimen differences are amplified for E_{APP} above about -0.800 V due to the sensitivity of crack tip H production and uptake to small changes in: (a) crack surface passivity (reduced by acidification and Cl$^-$ intrusion), and/or (b) the magnitude of crack tip potential reduction below E_{APP} (due to changing crack tip occlusion from corrosion product deposition [50]).

Considering classical plasticity analysis, the very low σ_H/σ_Y at x_{crit} of 1.0–2.0 μm (0.8–1.8, Table 1), or at the location of maximum stress ($r = 1.4$–12 μm, Fig. 4), provide poor predictions of K_{TH} and da/dt_{II} versus E_{APP}. Such predictions are similar to those from the lower σ_H/σ_Y SGP models in Figs. 5–8. Moreover, x_{crit} defined at the σ_H maximum, predicts da/dt_{II} that are substantially below measured values. Overall, the comparisons in Figs. 5–8 establish the necessity for high crack tip σ_H, equal or above $6\sigma_Y$, in order to predict the wide-range E_{APP} dependencies of K_{TH} and da/dt_{II} for steel. This result justifies both crack tip SGP and the relevance of the three-parameter PSGP formulation. However, this finding is problematic for K_{TH} modeling because Table 1 shows that σ_H/σ_Y above 6 is only predicted by the large strain FEA-PSGP analysis for K_I of 35–40 MPa$\sqrt{m}$. It is necessary to identify the cause of high crack tip stresses for K_I below 20 MPa$\sqrt{m}$.

It is difficult to justify very high crack tip stresses for ultra-high strength steel using the blunt crack PSGP approach *per se*. First, it is unlikely that the requirement for high crack tip stresses will be relaxed by changes in other aspects of the HEAC models. The parameters in the K_{TH} model (α'', β', and k_{IG} in (1)) and da/dt_{II} model ($D_{H\text{-EFF}}$ in (2)) were independently justified [46,47,51,53] and are consistent with the original analysis by Gerberich and coworkers [24,25,58]. Second, l_i is a primary

uncertainty in the PSGP and MSGP models, and has not been reported for ultra-high strength steel with a fine-scale martensitic structure and high ρ_S (10^{16} m^{-2} [75]) without strain hardening. As such, an SGP-FEA sensitivity study was conducted for a single K_I (20 MPa$\sqrt{m}$). In both SGP formulations, σ_H/σ_Y (at $r < 2$–5 μm) rises as l_{ref} increases from 1 to 15 μm. For example, at $r = 1$ μm, σ_H/σ_{YS} rises from 2.1 to 3.5 for MSGP and from 1.8 to 3.8 for PSGP, as l_i increases from 1 μm to 15 μm. These σ_H elevations do not achieve 6 to 7-times σ_Y, extending over r of 1–2 μm, as necessary to accurately predict E_{APP} dependent K_{TH} and da/dt$_{II}$ for Stage II K_I below about 30 MPa$\sqrt{m}$. There is no indication that alternate values of l_1, l_2, and l_3 yield such high crack tip stresses.

Other approaches predict high crack tip stresses, but only over distances that are small compared to an x$_{crit}$ of 1 μm. As an upper bound, σ_H from the singular terms of the plane strain elastic crack tip stress distribution is shown in Table 1. For the high strength steel, this stress exceeds $7\sigma_Y$ at $r = 1$ μm, but only for K_I above 33 MPa$\sqrt{m}$; even singular-elastic stresses are not sufficient. Dislocation free zone (DFZ) models show that the net crack tip stress field is reduced below the singular-elastic field [26,27]. The model represented by (1) is based on a DFZ approach, with the elastic crack tip stress field shielded by a pile-up of dislocations on a single slip plane coupled with a super-dislocation to capture the "far field" plastic zone [25]. Very high crack tip σ_H/σ_Y is predicted, but only over r less than 100 nm [24].

Enhancements to the continuum large-strain elastic-plastic SGP-FEA analysis could explain very high crack tip stresses extending of order ~1 μm ahead of the crack tip. The PSGP and MSGP stress fields (Figs. 1 and 4) were calculated for a smoothly blunting crack (e.g., Fig. 2a) [23]. SGP hardening is likely to be elevated for a geometrically "sharp" or irregular crack tip with reduced relaxation of the singularity. A tip that blunts to form a sharp corner could promote locally high stresses not relaxed by regular-geometric blunting [76]. Tip shape may be controlled by microstructural enforcement of the HEAC path, typically localized along austenite grain boundaries in Ni-superalloys and lath-martensite interfaces in modern steels. Slip morphology, influenced by HELP [9], could impact crack tip shape. *In situ* loading and SEM stereo imaging of transgranular fatigue crack and intergranular HEAC tips demonstrated much less blunting for the latter [77]. Alternately, microstructure-scale stresses can be elevated by slip morphology, dislocation substructure, and grain-elastic anisotropy [19]. Research must establish HEAC tip shape evolution over a range of K_I, and integrate local strain hardening due to SGP-GNDs with microstructure-scale stresses, all captured in a finite-strain crack tip FEA.

7. Conclusions

Large strain finite element analysis of crack tip stress, augmented by phenomenological and mechanism-based strain gradient plasticity formulations for a blunt crack, is integrated with electrochemical assessment of occluded-crack tip H solubility and H-decohesion based damage models to predict hydrogen assisted crack growth properties. Predictions agree with a robust data base for a high strength Ni superalloy and two modern ultra-high strength martensitic steels stressed in an aqueous H-producing environment. Conclusions are as follows.

- Large-strain FEA models establish a profound influence of SGP on crack tip stress and strain; GND density increases, crack tip stresses are elevated but do not exhibit a near-tip maximum, and crack opening is reduced compared to classical blunt-crack plasticity.

- The impact of SGP decreases with increasing alloy strength, but in all cases hydrostatic stress enhancement leads to locally high crack tip H concentration to enable damage; it is imperative to account for SGP hardening in modeling of H cracking.

- Integrated SGP, occluded-crack electrochemistry, and HEAC models effectively predict the dependencies of threshold stress intensity and H-diffusion limited Stage II crack growth rate on applied electrode potential for Monel®K-500 and ultra-high strength steel (AerMet™100 and Ferrium™M54) in NaCl solution with a single calibration constant.

- For Monel®K-500 with cathodic polarization, K_{TH} is accurately predicted using classical and SGP formulations of stress; however, Stage II crack growth rate is best predicted by the SGP descriptions that justify a critical distance of 1 μm due to crack tip stress elevation from GND hardening.

- For AerMet™100 and Ferrium™M54, measured and modeled K_{TH} and da/dt$_{II}$ quantitatively agree for cathodic and anodic potentials, within the bounds of somewhat uncertain crack tip H solubility, but only for crack tip σ_H/σ_Y of 6–8, which justifies SGP hardening and the relevance of a three-length PSGP model.

- Such high levels of crack tip σ_H/σ_Y, extending 1 μm beyond the crack tip, are not sufficiently predicted by PSGP simulation for low K_I typical of K_{TH} for the steels. The necessary-high stress is speculatively attributed to SGP interacting with crack tip geometry and/or HELP-sensitive microstructure-scale stresses.

References

[1] Modeling across Scales:A Roadmapping Study for Connecting Materials Models and Simulations across Length and Time Scales, The Minerals, Metals and Materials Society, Warrendale, PA, 2015.

[2] R.C. McClung, M.P. Enright, W. Liang, K. Chan, J. Moody, W.T. Wu, R. Shankar, W. Luo, J. Oh, S. Fitch, Integration of manufacturing process simulation with probabilistic damage tolerance analysis of aircraft engine components, in: 53rd AIAA/ASME/ASCE/AHS/ASC Structures, Structural Dynamics and Materials Conference, Honolulu, Hawaii, 2012. Paper No. AIAA 2012-1528.

[3] J.M. Papazian, E.L. Anagnostou, S.J. Engel, D. Hoitsma, J. Madsen, R.P. Silberstein, G. Welsh, J.B. Whiteside, A structural integrity prognosis system, Eng. Fract. Mech. 76 (2003) 51–59.

[4] P.L. Andresen, F.P. Ford, Prediction of stress corrosion cracking (SCC) in nuclear power systems, in: V.S. Raja, T. Shoji (Eds.), Stress Corrosion Cracking, Theory and Practice, Woodhead Publishing Limited, Cambridge (UK), 2011, pp. 651–713.

[5] R.P. Gangloff, Probabilistic fracture mechanics simulation of stress corrosion cracking using accelerated laboratory testing and multi-scale modeling, Corros. J. 72 (2016) 862–880.

[6] R.P. Gangloff, B.P. Somerday, Gaseous Hydrogen Embrittlement of Materials in Energy Technologies, vol. 1, Woodhead Publishing Limited, Cambridge (UK), 2012.

[7] R.P. Gangloff, Hydrogen assisted cracking of high strength alloys, in: I. Milne, R.O. Ritchie, B. Karihaloo (Eds.), Comprehensive Structural Integrity, Elsevier Science, New York, 2003, pp. 31–101.

[8] R.A. Oriani, Hydrogen, the versatile embrittler, Corrosion 4 (1987) 390–397.

[9] I.M. Robertson, P. Sofronis, A. Nagao, M.L. Martin, S. Wang, D.W. Gross, K.E. Nygren, Hydrogen embrittlement understood, Metall. Mater. Trans. A 46 (2015) 2323–2341.

[10] R.P. Wei, Fracture Mechanics: Integration of Mechanics, Materials Science and Chemistry, Cambridge University Press, New York, 2010.

[11] R.P. Gangloff, B.P. Somerday, Gaseous Hydrogen Embrittlement of Materials in Energy Technologies, vol. 2, Woodhead Publishing Limited, Cambridge (UK),

[12] M. Dadfarnia, A. Nagao, S. Wang, M.L. Martin, B.P. Somerday, P. Sofronis, Recent advances on hydrogen embrittlement of structural materials, Int. J. Fract. 196 (2015) 223—243.

[13] K.N. Akhurst, T.J. Baker, The threshold stress intensity for hydrogen-induced crack growth, Metall. Trans. A 12 (1981) 1059—1070.

[14] P. Novak, R. Yuan, B.P. Somerday, P. Sofronis, R.O. Ritchie, A statistical physical-based, micro-mechanical model of hydrogen-induced intergranular fracture in steel, J. Mech. Phys. Solids 58 (2010) 206—226.

[15] M. Dadfarnia, B.P. Somerday, P.E. Schembri, P. Sofronis, J.W. Foulk, K.A. Nibur, D.K. Balch, On modeling hydrogen-induced crack propagation under sustained load, JOM 66 (2014) 1390—1398.

[16] D. Lee, Y. Huang, J.D. Achenbach, A comprehensive analysis of the growth rates of stress corrosion cracks, Proc. R. Soc. A 471 (2015) 20140703.

[17] S. Serebrinsky, E. Carter, M. Ortiz, A quantum-mechanically informed continuum model of hydrogen embrittlement, J. Mech. Phys. Solids 52 (2004) 2403—2430.

[18] M.M. Hall Jr., D.M. Symons, Hydrogen assisted creep fracture model for low potential stress corrosion cracking of Ni-Cr-Fe alloys, in: R.H. Jones (Ed.), Chemistry and Electrochemistry of Stress Corrosion Cracking, the Minerals, Metals & Materials Society, Warrendale, 2001, pp. 447—466.

[19] Q. Wu, M.A. Zikry, Prediction of diffusion assisted hdyrogen embrittlement failure in high strength martenitic steels, J. Mech. Phys. Solids 85 (2015) 143—159.

[20] A.H. Krom, R.W.J. Koers, A. Bakker, Hydrogen transport near a blunting crack tip, J. Mech. Phys. Solids 47 (1999) 971—992.

[21] A. Taha, P. Sofronis, A micromechanics approach to the study of hydrogen transport and embrittlement, Eng. Fract. Mech. 68 (2001) 803—837.

[22] J.R. Rice, Mechanics aspects of stress corrosion cracking and hydrogen embrittlement, in: R.W. Staehle, et al. (Eds.), Stress Corrosion Cracking and Hydrogen Embrittlement of Iron Base Alloys, NACE International, Houston, 1977, pp. 11—15.

[23] R.M. McMeeking, Finite deformation analysis of crack-tip opening in elastic-plastic materials and implications for fracture, J. Mech. Phys. Solids 25 (1977) 357—381.

[24] W.W. Gerberich, R. Oriani, M.-J. Lii, X. Chen, T. Foecke, The necessity of both plasticity and britleness in the fracture thresholds of iron, Philos. Mag. A 63 (1991) 363—376.

[25] W.W. Gerberich, Modeling hydrogen induced damage mechanisms in metals, in: R.P. Gangloff, B.P. Somerday (Eds.), Gaseous Hydrogen Embrittlement of Materials in Energy Technologies, vol. 2, Woodhead Publishing Ltd, Cambridge, 2012, pp. 209—246.

[26] S.M. Ohr, Dislocation-crack interaction, J. Phys. Chem. Solids 48 (1987) 1007—1014.

[27] J. Chen, S. Kitaoka, Distribution of dislocations at a mode I crack tip and their shielding effect, Int. J. Fract. 100 (1999) 307—320.

[28] J.P. Hirth, Effects of hydrogen on the properties of iron and steel, Metall. Trans. A 11 (1980) 861—890.

[29] T.-Y. Zhang, J.E. Hack, The equilibrium concentration of hydrogen atoms ahead of a mixed mode I-Mode III crack tip in single crystal iron, Metall. Mater. Trans. A 30 (1999) 155—159.

[30] J.S. Stölken, A.G. Evans, A microbend test method for measuring the plasticity length scale, Acta Mater 46 (1998) 5109—5115.

[31] N.A. Fleck, J.W. Hutchinson, A reformulation of strain gradient plasticity, J. Mech. Phys. Solids 49 (2001) 2245—2271.

[32] L. Bardella, A. Panteghini, Modelling the torsion of thin metal wires by distortion gradient plasticity, J. Mech. Phys. Solids 78 (2015) 467—492.

[33] H. Gao, Y. Huang, W.D. Nix, J.W. Hutchinson, Mechanism-based strain gradient plasticity - I. Theory, J. Mech. Phys. Solids 47 (1999) 1239—1263.

[34] Y. Huang, S. Qu, K.C. Hwang, M. Li, H. Gao, A conventional theory of mechanism-based strain gradient plasticity, Int. J. Plast. 20 (2004) 753—782.

[35] E. Martínez-Pañeda, C.F. Niordson, L. Bardella, A finite element framework for distortion gradient plasticity with applications to bending of thin foils, Int. J. Solids Struct. (2016), http://dx.doi.org/10.1016/j.ijsolstr.2016.06.001.

[36] U. Komaragiri, S.R. Agnew, R.P. Gangloff, M.R. Begley, The role of macroscopic hardening and individual length-scales on crack tip stress elevation from phenomenological strain gradient plasticity, J. Mech. Phys. Solids 56 (2008) 3527—3540.

[37] E. Martínez-Pañeda, C. Betegón, Modeling damage and fracture within strain-gradient plasticity, Int. J. Solids Struct. 59 (2015) 208—215.

[38] E. Martínez-Pañeda, C.F. Niordson, On fracture in finite strain gradient plasticity, Int. J. Plast. 80 (2016) 154—167.

[39] M.R. Begley, J.A. Begley, C.M. Landis, Continuum mechanics modeling of hydrogen embrittlement, in: R.P. Gangloff, B.P. Somerday (Eds.), Gaseous Hydrogen Embrittlement of Materials in Energy Technologies, vol. 1, Woodhead Publishing Ltd, Cambridge, 2012, pp. 286—325.

[40] D. Korn, G. Elssner, R.M. Cannon, M. Rühle, Fracture properties of interfacially doped Nb-Al$_2$O$_3$ bicrystals: I, fracture characteristics, Acta Mater 50 (2002) 3881—3901.

[41] R.H. Dauskardt, M. Lane, Q. Ma, N. Krishna, Adhesion and debonding of multi-layer thin film structures, Eng. Fract. Mech. 61 (1998) 142—162.

[42] N.C. Broedling, A. Hartmaier, H. Gao, Fracture toughness of layered structures: embrittlement due to confinement of plasticity, Eng. Fract. Mech. 75 (2008) 3743—3754.

[43] P.F. Thomason, Ductile Fracture of Metals, Pergamon Press, Oxford, 1990.

[44] S. Brinckmann, T. Siegmund, Computations of fatigue crack growth with strain gradient plasticity and an irreversible cohesive zone model, Eng. Fract. Mech. 75 (2008) 2276—2294.

[45] E. Martínez-Pañeda, S. del Busto, C.F. Niordson, C. Betegón, Strain gradient plasticity modeling of hydrogen diffusion to the crack tip, Int. J. Hydrogen Energy 41 (2016) 10265—10274.

[46] R.P. Gangloff, H.M. Ha, J.T. Burns, J.R. Scully, Measurement and modeling of hydrogen environment-assisted cracking in Monel K-500, Metall. Mater. Trans. A 45 (2014) 3814—3833.

[47] J.T. Burns, Z.D. Harris, J.D. Dolph, R.P. Gangloff, Measurement and modeling of hydrogen environment assisted cracking in a Ni-Cu-Al-Ti superalloy, Metall. Mater. Trans. A 47 (2016) 990—997.

[48] G.L. Pioszak, Metallurgical Control of Stress Corrosion Cracking in Ultra-high Strength Stainless Steel, PhD Dissertation, University of Virginia, Charlottesville, VA, 2015.

[49] Y. Lee, R.P. Gangloff, Measurment and modeling of hydrogen environment-assisted cracking of ultra-high strength steels, Metall. Mater. Trans. A 38 (2007) 2174—2190.

[50] B.A. Kehler, J.R. Scully, Predicting the effect of applied potential on crack tip hydrogen concentration in low-alloy martensitic steels, Corros. J. 64 (2008) 465—477.

[51] J. Ai, H. Ha, R.P. Gangloff, J.R. Scully, Hydrogen diffusion and trapping in a precipitation-hardened nickel-copper-aluminum alloy Monel K-500, Acta Mater 61 (2013) 3186—3199.

[52] D. Li, R.P. Gangloff, J.R. Scully, Hydrogen trap states in ultrahigh-strength AerMet® 100 steel, Metall. Mater. Trans. A 35 (2004) 849—964.

[53] D. Figueroa, M.J. Robinson, Hydrogen transport and embrittlement in 300M and AerMet™100 ultra high strength steels, Corros. Sci. 52 (2010) 1593—1602.

[54] G.K. Dey, P. Mukhapadhyay, Precipitation hardening in nickel-copper base alloy Monel K-500, Mater. Sci. Engr. 84 (1986) 177—189.

[55] R. Ayer, P. Machmeier, Transmission electron microscopy examination of hardening and toughening phenomena in AerMet100, Metall. Trans. A 24A (1993) 1943—1995.

[56] C. Wang, C. Zhang, Z. Yang, Austenite layer and precipitation in high Co-Ni maraging steel, Micron 67 (2014) 112—116.

[57] T.L. Anderson, Fracture Mechanics — Fundamentals and Applications, Taylor and Francis Group, Boca Raton, FL, 2005, p. 111.

[58] H. Huang, W.W. Gerberich, Quasi-equilibrium modeling of toughness transition during semibrittle cleavage, Acta Metall. Mater 42 (1994) 639—647.

[59] P. Doig, G.T. Jones, A model for the initiation of hydrogen embrittlement cracking at notches in gaseous hydrogen environments, Metall. Trans. A 8 (1977) 1993—1998.

[60] R.P. Gangloff, Diffusion control of hydrogen environment embrittlement in high strength alloys, in: N.R. Moody, et al. (Eds.), Hydrogen Effects on Material Behavior and Corrosion Deformation Interactions, The Minerals, Metals & Materials Society, Warrendale, 2003, pp. 477—497.

[61] E. Akiyama, M. Wang, S. Li, Z. Zhang, Y. Kimura, N. Uno, K. Tsuzaki, Studies of the evaluation of hydrogen embrittlement property of high-strength steels with consideration of the effect of atmospheric corrosion, Metall. Mater. Trans. A 44 (2012) 1290—1300.

[62] M.R. Begley, J.W. Hutchinson, The mechanics of size-dependent indentation, J. Mech. Phys. Solids 46 (1998) 2049—2068.

[63] Y.J. Ro, M.R. Begley, R.P. Gangloff, S.R. Agnew, Effect of aging on scale-dependent plasticity in aluminum alloy 2024 and implications for crack tip damage, Mater. Sci. Eng. A 435—436 (2006) 332—342.

[64] X. Qian, S. Zhang, S. Swaddiwudhipong, L. Shen, Temperature dependence of material length scale for strain gradient plasticity and its effect on near-tip opening displacement, Fatigue Fract. Eng. Mater. Struct. 37 (2014) 157—170.

[65] S. Schonecker, S.K. Kwon, B. Johansson, L. Vitos, Surface parameters of ferritic iron-rich Fe-Cr alloy, J. Phys. Condens. Matter 25 (2013) 305002.

[66] R. Chait, Factors influencing the strength differential of high strength steels, Metall. Trans. 3 (1972) 369—375.

[67] T. Lin, A.G. Evans, R.O. Ritchie, A statisitical model of brittle fracture by transgranular cleavage, J. Mech. Phys. Solids 34 (1986) 477—497.

[68] W.W. Gerberich, P.G. Marsh, H. Huang, The effect of local dislocation arrangements on hydrogen-induced cleavage, in: S. Breumer, et al. (Eds.), Fundamental Aspects of Stress Corrosion Cracking, TMS-AIME, Warrendale, PA, 1992, pp. 191—204.

[69] S. Lynch, Mechanisitc and fractographic aspects of stress corrosion cracking, Corros. Rev. 30 (2012) 63—104.

[70] A. Turnbull, Hydrogen diffusion and trapping in metals, in: R.P. Gangloff, B.P. Somerday (Eds.), Gaseous Hydrogen Embrittlement of Materials in Energy Technologies, vol. 1, Woodhead Publishing Ltd, Cambridge (UK), 2012, pp. 89—128.

[71] J. Toribio, V. Kharin, A generalized model of hydrogen diffusion in metals with multiple trap types, Philos. Mag. 95 (2015) 3429—3451.

[72] W.C. Johnson, J.Y. Huh, Thermodynamics of stress-induced interstitial redistribution in bcc metals, Metall. Mater. Trans. A 34 (2003) 2819—2825.

[73] R.L.S. Thomas, J.R. Scully, R.P. Gangloff, Internal hydrogen embrittlement of ultrahigh-strength AerMet®100 Steel, Metall. Mater. Trans. A 34 (2003) 327—344.

[74] J.R. Scully, P.J. Moran, The influence of strain on hydrogen entry and transport in a high strength steel in sodium chloride solution, J. Electrochem. Soc. 135 (1988) 1337—1348.

[75] S. Takebayuashi, T. Kunieda, N. Yoshinaga, K. Ushioda, S. Ogata, Comparison of the dislocation density in martensitic steels evaluated by some X-ray diffraction methods, ISIJ Int. 50 (2010) 875—882.

[76] K.J. Handerhan, W.M. Garrison Jr., A study of crack tip blunting and the influence of blunting behavior on the fracture toughness of ultra high strength steels, Acta Metall. Mater 40 (1992) 1337—1355.

[77] B.P. Somerday, L.M. Young, R.P. Gangloff, Crack tip mechanics effects on environment-assisted cracking of beta-titanium alloys in aqueous NaCl, Fatigue frac. Eng. Mater. Struct. 23 (2000) 39—58.